Materials & Design 265 (2026) 115843

Contents lists available at ScienceDirect

Materials & Design

journal homepage: www.elsevier.com/locate/matdes

Chiral Carbon Quantum Dots with High-Specificity Report Function as Efficient Antimicrobial Nanoagent to Resist Antibiotic Resistance

Lina Wu [a,1], Xiaoyun Lin [b,1], Lingxuan Sun [a], Jinpin Zhang [a], Jinxi Liu [a], Shuixin Liang [a], Wei Luo [a], Jiaxin Xue [a], Yujun Wen [c], Tiantian Wang [e], Ailin Liu [c], Yong Diao [a], Xianquan Feng [d,*], Liqing Lin [c,*]

[a] School of Biomedical Science, Huaqiao University, Quanzhou 362021, China
[b] Department of Pharmacy, Shengli Clinical Medical College of Fujian Medical University, Fujian Provincial Hospital, Fuzhou University Affiliated Provincial Hospital, Fuzhou 350001, China
[c] Department of Pharmaceutical Analysis, School of Pharmacy, Fujian Medical University, Fuzhou 350122, China
[d] Fujian Provincial Key Laboratory of Transplant Biology of Laboratory of Basic Medicine, Fuzong Clinical Medical College of Fujian Medical University, 900th Hospital of PLA Joint Logistic Support Force, Fuzhou 350025, China
[e] Xizang Qamdo City Maternal and Child Health Hospital, Qamdo 854000, Xizang Autonomous Region, China

ARTICLE INFO

Keywords:
Chiral carbon quantum dots
Levofloxacin
D-histidine
Antimicrobial activity
Antibiotic resistance

ABSTRACT

To address the growing challenge of bacterial antibiotic resistance, this study designed and synthesized chiral carbon quantum dots (h-DCQDs) from levofloxacin and D-histidine. The h-DCQDs exhibit strong broad-spectrum antibacterial activity against both Gram-positive and Gram-negative bacteria, while also inhibiting the development of bacterial resistance and promoting wound healing. The antibacterial mechanism of h-DCQDs involves reactive oxygen species generation and specific interaction with bacterial cell walls/membranes, leading to structural disruption, content leakage, and cell death. Owing to their excellent biocompatibility and fluorescence, h-DCQDs can also serve as effective bacterial imaging probes. This work highlights the innovation of using chiral carbon quantum dots, which achieve bacteria-specific targeting and integrate antimicrobial and reporting functions. This offers a promising strategy for tracking and treating bacterial infections.

1. Introduction

The rise of antibiotic resistance constitutes a global public health crisis, driven by the misuse of antimicrobials and leading to persistent, recurrent infections and the spread of multidrug-resistant pathogens [1]. Conventional antibiotic therapies are increasingly challenged by poor drug penetration and biofilm-mediated resistance, underscoring an urgent need for novel antibacterial systems that combine potent bactericidal activity with precise targeting capabilities [2]. Nanomaterials, particularly carbon quantum dots (CQDs), have emerged as a promising platform to address this dilemma due to their excellent biocompatibility, ease of synthesis, and low propensity to induce bacterial resistance [3,4]. The structural and optical properties of CQDs are highly tunable through synthesis parameter adjustments and surface engineering [5,6], which directly influences their interactions with bacterial cells [7]. A key strategy to enhance specificity is the incorporation of chiral motifs, such as D-amino acids (enantiomeric amino acids with a D-configuration), known for their targeting affinity towards bacterial cell walls and metabolic pathways [8]. For instance, D-amino acid conjugates and chiral CQDs derived from D-cysteine [9] or D-glutamine [10] have demonstrated improved bacterial targeting. This specificity stems from the preferential interaction of D-enantiomers with bacterial peptidoglycan, making them valuable for medical applications [11]. Furthermore, such chiral CQDs can intercalate into bacterial DNA, causing topological damage [12].

Concurrently, the intrinsic fluorescence of CQDs enables their use as probes for bacterial detection and imaging [13,14]. While antibiotic-derived fluorescent probes offer inherent targeting [15], their utility can be limited by pathogen susceptibility [16]. Therefore, integrating a reporting function into antibacterial CQDs presents a promising theranostic strategy for infection monitoring [17]. The antibacterial action of CQDs often involves the generation of reactive oxygen species (ROS),

* Corresponding authors.
E-mail addresses: fxq6013@fjmu.edu.cn (X. Feng), liqinglin@fjmu.edu.cn (L. Lin).
[1] These authors contributed equally to this work.

https://doi.org/10.1016/j.matdes.2026.115843
Received 22 October 2025; Received in revised form 12 February 2026; Accepted 12 March 2026
Available online 13 March 2026

damaging bacterial membranes and internal components [18]. Nitrogen-rich precursors can enhance this ROS production [19]. Although antibiotic-based CQDs like those from levofloxacin show potent activity [20], their development as integrated platforms for specific targeting, real-time imaging, and robust anti-biofilm application remains insufficiently explored.

Herein, we identify a critical research gap: the lack of chiral carbon quantum dots that simultaneously possess high targeting specificity, a built-in reporting capability, and effective anti-resistance properties, particularly against resilient biofilms. To bridge this gap, we present the rational design, synthesis, and mechanism of bacteria-targeting chiral carbon quantum dots (h-DCQDs) with a high-specificity reporting function for antibacterial and antibiofilm applications (Fig. 1). The h-DCQDs are synthesized from levofloxacin and D-histidine, strategically combining the broad-spectrum antibacterial activity of the fluoroquinolone with the bacterial targeting and chiral signature of the D-amino acid. This work demonstrates that the resulting h-DCQDs exhibit selective broad-spectrum antibacterial activity, excellent biocompatibility, and potent antibiofilm efficacy. The primary antibacterial mechanism is attributed to ROS generation upon bacterial attachment, leading to outer membrane disruption and content leakage. The innovation and significance of this work lie in the creation of a multifunctional theranostic agent that serves as both a fluorescent probe for monitoring and a nano-antibiotic for combatting bacterial infections, offering a promising strategy to monitor and reverse antibiotic resistance.

2. Experiment section

2.1. Preparation of different DCQDs

A series of D-amino acid functionalized carbon quantum dots (DCQDs) were prepared by one-step hydrothermal method as reported in previous research. Specifically, levofloxacin and D-amino acid, including D-histidine (D-his), D-arginine (D-arg), D-lysine (D-lys), D-tyrosine (D-tyr), D-aspartic acid (D-asp), D-alanine (D-ala), D-methionine (D-met), D-phenylalanine (D-phe), D-leucine (D-leu), D-threonine (D-thr) and L-histidine (L-his) were prepared previously. Then, the raw materials including levofloxacin and D-amino acid were dissolved in deionized water and transferred into Teflon-lined autoclaves and heated at 200 ℃ for 12 h. After the reaction finished, the solution was cooled down to room temperature, purified through centrifugal filter, dialyzed by membrane of 100–500 Da and lyophilized to obtain DCQDs powders for further used.

2.2. Statistical analysis

All data were acquired with parallel experiment. All statistical analyses were performed with Student's *t*-test using GraphPad Prism 8. $P < 0.05$ was considered as a statistically significant difference.

3. Results and discussion

3.1. Synthesis and characterization of h-DCQDs

The carbon quantum dots were synthesized through a facile hydrothermal approach, which derived from different types of D-type amino acids and levofloxacin. We measured the minimum inhibitory concentration values of all the synthesized carbon quantum dots against three representative strains, including *Staphylococcus aureus* (*S. aureus*), methicillin-resistant *Staphylococcus aureus* (MRSA), and *Escherichia coli* (*E. coli*). The results showed that the h-DCQDs (levofloxacin + D-tryptophan) had the lowest minimum inhibitory concentration (0.025–0.05 μg/ml) and the highest biofilm clearance rate (≥90%), indicating that D-tryptophan was the optimal chiral precursor. The screening results are summarized in Table S1. Fluorescence properties and antibacterial activities of h-DCQDs could be affected by various factors, such as the solvent ratio, reaction temperature, and reaction time. Based on the results of optimization and antibacterial activity, the optimal preparation conditions were as follows: a solvent ratio of 1:1 (with 0.2 g of levofloxacin and 0.2 g of D-histidine), a reaction temperature of 200°C, and a reaction time of 12 h, respectively (Fig. S1).

Transmission electron microscopy (TEM) images revealed that the h-DCQDs exhibited a spherical morphology and a homogeneous size

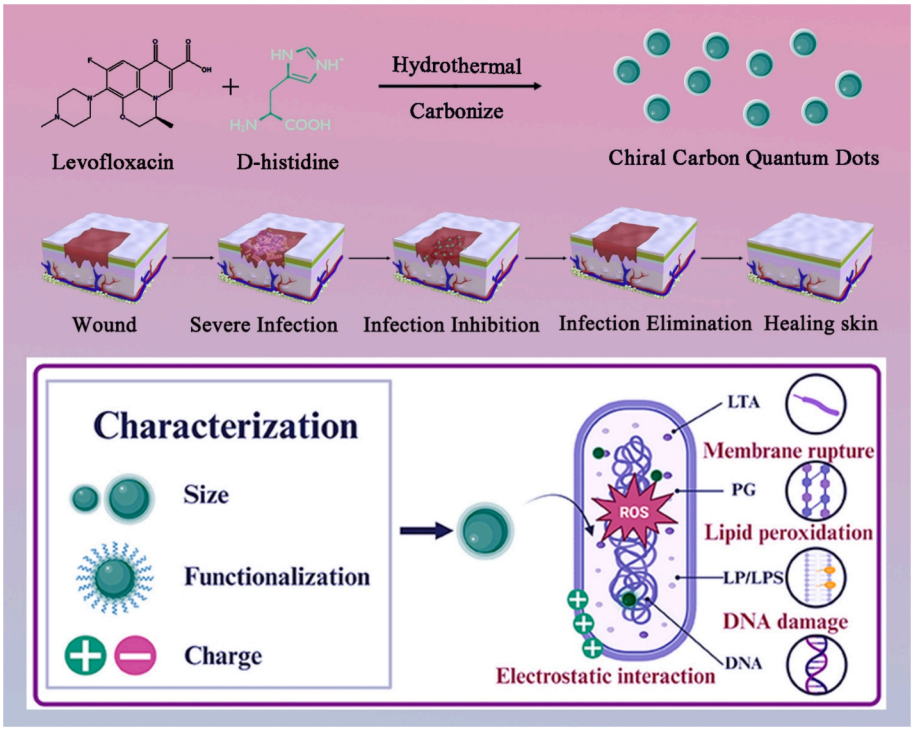

Fig. 1. Schematic illustration of the synthesis and proposed antibacterial mechanism of the chiral carbon quantum dots (h-DCQDs).

distribution (Fig. 2A), and their corresponding size distribution with a diameter of 1.0 ± 0.22 nm was shown in Fig. 2D. The size distribution analysis of h-DCQDs in the TEM images (Fig. 2B) demonstrated that h-DCQDs possessed good monodispersity. The intercrystalline spacing of h-DCQDs was measured to be 0.22 nm, which corresponded to a well-resolved lattice fringe (Fig. 2C, inset). Dynamic light scattering (DLS) measurements indicated that the particle size of h-DCQDs in water was 3.35 ± 0.15 nm (Fig. S2A). The difference between DLS and TEM results is due to the fact that DLS measures the hydrodynamic diameter including the solvent layer on the surface of h-DCQDs, while TEM reflects the actual core size of the nanoparticles. Additionally, the ζ-potential of h-DCQDs was determined to be positive (39.87 ± 0.73 mV) by DLS, which was likely due to the protonation of the amino groups on the surface of h-DCQDs (Fig. S2B). Through the investigation of size and surface charge, the preliminary morphological characteristics of h-DCQDs were elucidated.

The composition and structure of h-DCQDs were further investigated by the UV–vis spectra. As shown in Fig. 2E, the absorption peak at 220 nm is assigned to D-histidine, while those at 240 nm, 295 nm and 340 nm are ascribed to levofloxacin. After the preparation of h-DCQDs using levofloxacin and D-histidine as precursors, the absorption peak originally at 220 nm undergoes a red shift to 250 nm, and the peak at 295 nm shifts to 300 nm, which is associated with the π-π* transition of the carbonyl group in D-histidine [21]. Notably, the absorption peak in the range of 295–300 nm corresponds to the π-π* transition of the imidazole ring in histidine, representing a characteristic absorption peak of histidine and its derivatives [22]. To further verify the specificity of this characteristic peak, a comparative experiment was conducted using carbon quantum dots synthesized without histidine but using levofloxacin alone (LCDs) exhibit no absorption peak at 295–300 nm [20]. Concurrently, the absorbance of the negligible band in the range of 360 nm and 500 nm was connected to the surface and edge defects of h-DCQDs. The internal illustration was the optical photographs of h-DCQDs solution at pH 7.4 under light and 365 nm ultraviolet light illumination, as shown in the inset of Fig. 2E. Furthermore, the photoluminescence spectra of the synthesized h-DCQDs were shown in Fig. 2F. h-DCQDs emitted the strongest fluorescence spectra at 497 nm under the excitation at 340 nm. Meanwhile, the small change was observed in the emission under the excitation from 220 to 440 nm (Fig. S2C). The average fluorescence lifetime of the h-DCQDs was 6.99 ns (Fig. S2D), which could target molecules to distinguish even in the case of background fluorescence interference for relatively long fluorescence lifetime having higher sensitivity in fluorescence detection.

The main groups of raw materials, h-LCQDs and h-DCQDs were characterized by FTIR (Fig. 3A and B). The absorption bimodal peaks of $–NH_2$ groups at 3400–3200 cm^{-1} appeared in h-LCQDs and h-DCQDs. The N-H bending at 1689 cm^{-1} appeared in D-histidine and h-LCQDs and h-DCQDs [22]. The absorption peaks of h-LCQDs and h-DCQDs at 700–1000 cm^{-1} were attributed to the C-O and C-C bond stretching vibration. The high temperature conditions of synthesis resulted in various oxidation states on the surface of h-LCQDs and h-DCQDs. Meanwhile, the characteristic peak of the imidazole ring (770 cm^{-1}) indicated that the core structure of the chiral source (L/D-histidine) remained intact during synthesis, providing a structural basis for the handedness of h-LCQDs and h-DCQDs [23]. Fig. 3C further showed the XPS spectrum of h-DCQDs. The results of XPS analysis indicated that the as-prepared h-DCQDs were composed of four elements: C, N, O and F (Fig. 3C). The C1s XPS at 284.78 eV, 286.09 eV and 288.27 eV of h-DCQDs indicated that −C-C, –CN and –COOH existed in h-DCQDs [24] (Fig. 3D). The peaks of N 1 s at 398.98 eV and 401.08 eV indicated the existence of Pyridinic N and $–NH_2$ [25] (Fig. 3E). The peaks of O 1 s at 531.08 eV and 532.98 eV of h-DCQDs could be divided into two peaks, belonging to −C=O-N and –COOH [26], respectively (Fig. 3F). The peaks of F 1 s at 687.08 eV and 688.62 eV of h-DCQDs could be divided into two peaks, belonging to −CF and −C-CF [27], respectively (Fig. 3G). The representation means of FTIR and XPS effectively characterized the types of functional groups, especially –COOH and $–NH_2$, which demonstrated the successful synthesis of h-DCQDs. These spectra results of h-LCQDs and h-DCQDs confirmed that h-LCQDs and h-DCQDs possess identical chemical structures [28]. The hydrothermal synthesis

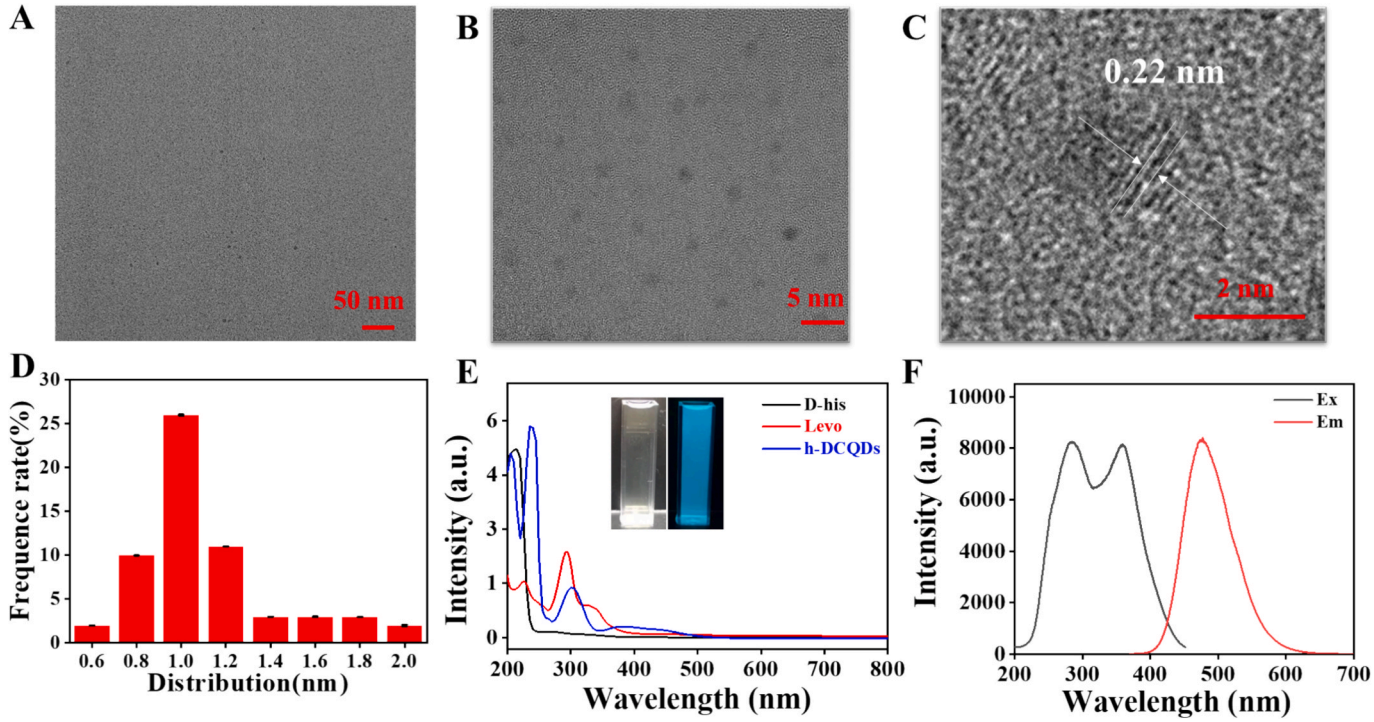

Fig. 2. The characterization of h-DCQDs. (A) The large and (B) small field of view TEM image of (C) HR-TEM images of h-DCQDs, scale bar: 50 nm, 5 nm, and 2 nm, respectively. (D) The corresponding size distribution of h-DCQDs in TEM vision of image A. (E) UV–vis absorption spectra of h-DCQDs. (F) Excitation-emission matrix spectra of h-DCQDs solution.

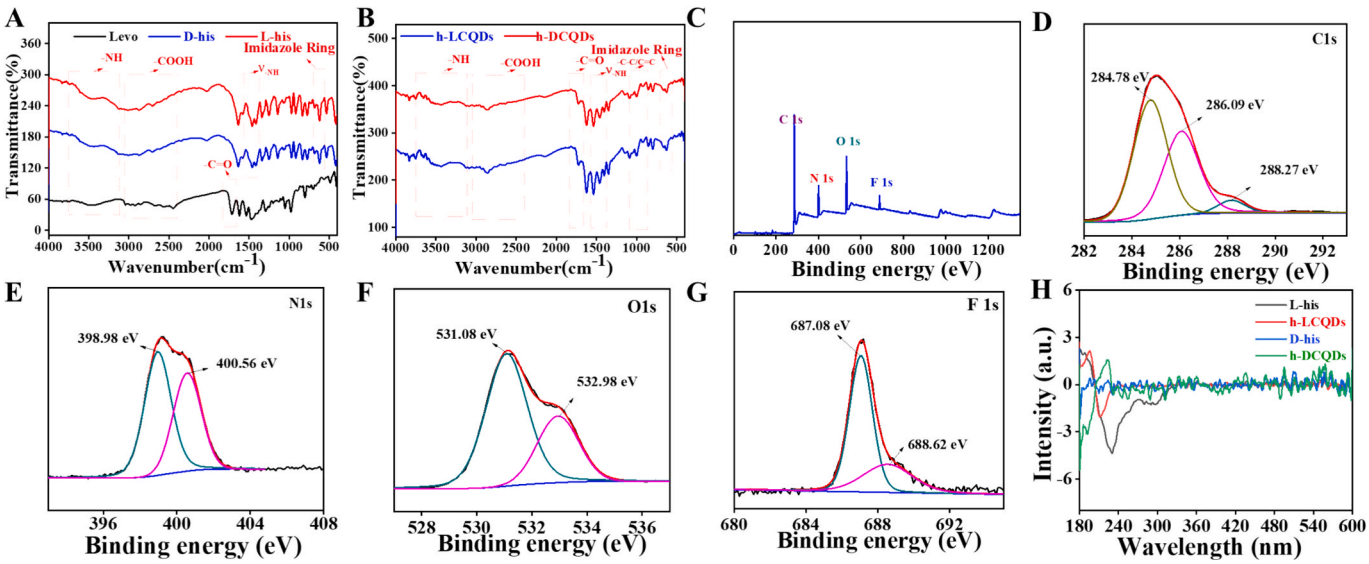

Fig. 3. The surface group characterization of h-DCQDs. (A) FTIR spectrum of Levo, L-his, and D-his, (B) FTIR spectrum of h-LCQDs, and h-DCQDs, (C) XPS spectrum of h-DCQDs, (D) C1s, (E) N1s, (F) O1s, and (G) F1s spectrogram of XPS spectrum of h-DCQDs, (H) CD spectra of L-his, h-LCQDs, D-his, and h-DCQDs.

of chiral carbon quantum dots could keep the chiral center of amino acid raw materials well [29]. The circular dichroism (CD) spectra of h-LCQDs and h-DCQDs exhibit opposite optical activity, confirming their mirror-symmetric chiral configurations [23]. The h-DCQDs retained the chiral characteristics of amino acid raw materials and the absorption of circularly polarized light is consistent with the raw materials in the 200–300 nm range, which could also infer the structural information of h-DCQDs chiral molecules (Fig. 3H). It could be inferred that the D-histidine served as a chiral inducer with its chiral information being imprinted into the carbon framework of h-DCQDs [30] and the signals of h-DCQDs chiral molecules formed from the surface and inside of h-DCQDs [9]. The above results showed that h-DCQDs were formed with plenty of functional groups, especially –COOH, $–NH_2$ and chirality group.

3.2. *Fluorescence imaging of h-DCQDs*

Bioimaging plays a crucial role in numerous pathological and biological processes. Before the imaging ability of h-DCQDs was investigated, the fluorescence quantum yield of h-DCQDs was studied, which

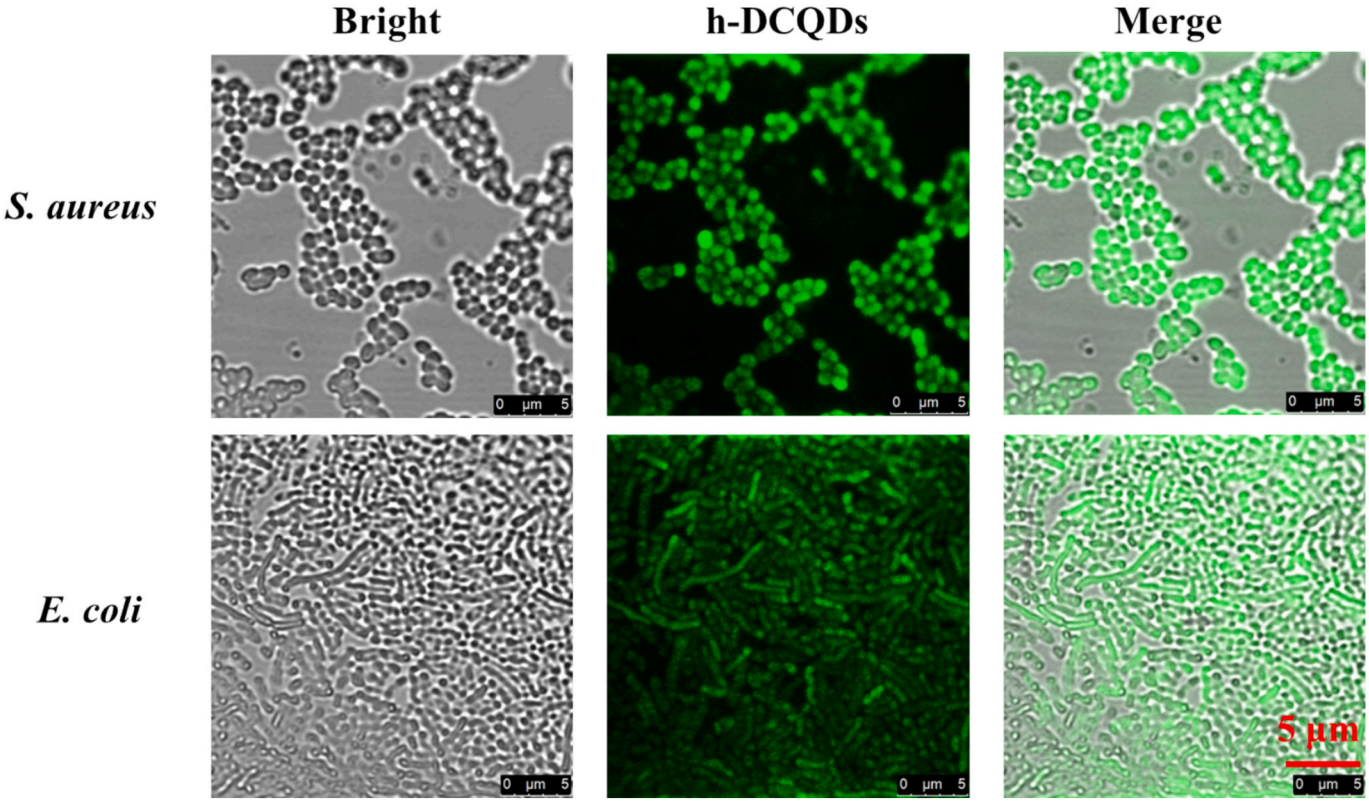

Fig. 4. The imaging effect in bacteria of h-DCQDs. Imaging effect of h-DCQDs in *S. aureus* and *E. coli* with the excitation wavelength of 405 nm, scale bar: 5 μm.

can affect the efficiency and performance of fluorescent materials in various applications. Comparing the fluorescence sample to be detected with the reference sample 6 RG, as shown in Fig. S3A, the fluorescence quantum yield of h-DCQDs was calculated to be 23.79%, which showed excellent fluorescence effect of h-DCQDs for imaging. Meanwhile, the photostability of h-DCQDs is one of the important parameters to evaluate the performance of fluorescent materials. The photostability experiment showed that the fluorescence intensity of h-DCQDs was highly stable even when it was continuously excited by a 125 W mercury lamp for 3600 s (Fig. S3B). As shown in Fig. 4, the imaging ability of h-DCQDs in both *S. aureus* and *E. coli* was excellent. With the increase of incubation time, the effect of bacterial imaging became gradually clearer (Fig. S3C). The above results showed that h-DCQDs was a promising biological imaging material.

3.3. Antibacterial and anti-biofilm of h-DCQDs in vitro

According to the previous antibacterial activity experimental results of levofloxacin-based carbon quantum dots [32], h-DCQDs derived from levofloxacin and D-histidine also might be used as an effective antibacterial agent. The antibacterial activity of h-DCQDs against different bacteria *in vitro* was evaluated according to the disk diffusion method, which was carried out with LB agar plate. Paper pieces were placed on the LB agar plate with levofloxacin-based carbon quantum dots, D-histidine and h-DCQDs, respectively. The antibacterial activity of h-DCQDs could be evaluated by forming an obvious bacteriostatic zone after 20 h. As shown in Fig. 5A and B, h-DCQDs showed significantly higher antibacterial activity than levofloxacin-based carbon quantum dots. However, there was scarcely any bacteriostatic circle for D-histidine. Meanwhile, the synthesized CQDs from only D/L-his (denoted as h-CQDs) and only levofloxacin (denoted as LCDs) using the same method, the MIC values of which against *S. aureus*, MRSA, and *E. coli*, the supplementary data are presented in Table S2. The biofilm clearance rate of h-CQDs, LCDs, h-LCQDs, and h-DCQDs against *S. aureus*, MRSA, and *E. coli* was presented in Fig. S4. Compared with h-DCQDs, the results show that h-DCQDs have significantly higher antibacterial, confirming that D-his and its chiral properties enhance the biological activity of the material. The superior performance of h-DCQDs may be attributed to the synergistic effects of the carbon quantum dot matrix and the D-his modification. The enhanced antibacterial activity of h-DCQDs might result from the decrease of size and the increase of targeted binding force to bacteria, which was investigated by the CD spectra (Fig. 3H). The cell wall of bacteria contains peptidoglycan, which is an important structural component and is essential for the growth and survival of bacteria. In the process of peptidoglycan synthesis, there is an enzyme called MurD ligase, which has high stereoselectivity to D-amino acid [31]. By designing specific carbon dots, these carbon dots mimic D-amino acids in structure and can specifically bind to MurD ligase in peptidoglycan synthesis pathway in bacterial cell wall. This combination prevents the normal function of MurD ligase, thus significantly inhibiting the synthesis of peptidoglycan. Because peptidoglycan is the main component of bacterial cell wall, its synthesis is blocked, which will lead to the abnormal formation of cell wall to destroy the integrity of bacterial cells and eventually lead to bacterial death. The minimum

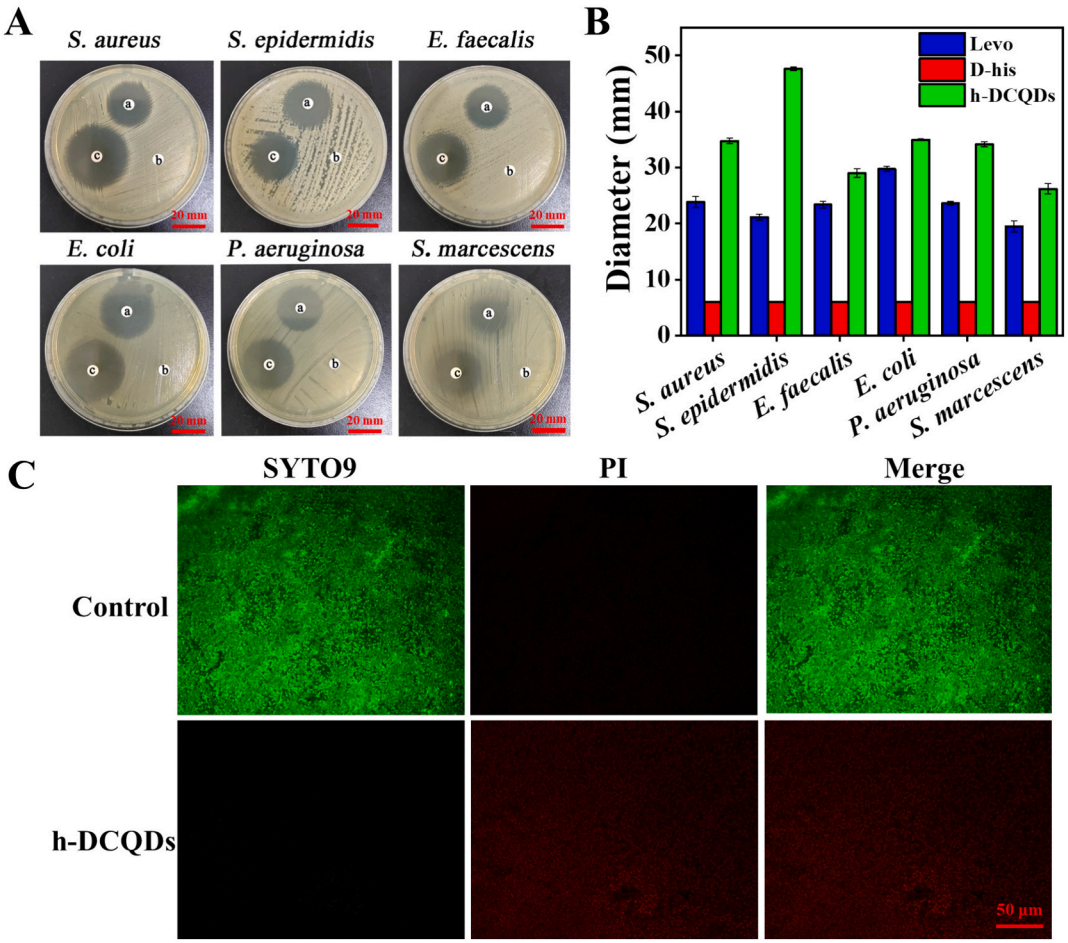

Fig. 5. The antibacterial ability of h-DCQDs. (A) The antibacterial ability of h-DCQDs with Disk-Diffusion Method, (a) levofloxacin-based carbon quantum dots, (b) D-histidine, and (c) h-DCQDs, scale bar: 20 nm. (B) The quantitative data of bacteriostatic circle against different bacteria of h-DCQDs, including *S. aureus*, *S. epidermidis*, *E. faecalis*, *E. coli*, *P. aeruginosa* and *S. marcescens*. (C) Live/dead bacteria imaging of *S. aureus* incubated with h-DCQDs, scale bar: 50 μm.

inhibitory concentration (MIC) and minimum bactericidal concentration (MBC) values for different strains (*S. aureus*, MRSA, and *E. coli*) using h-DCQDs have been determined and are presented in Table 1. Meanwhile, the bacteriostatic curve of h-DCQDs against *S. aureus*, MRSA and *E. coli* was carried out by broth microdilution method and consistent with the disk diffusion method, as shown in Fig. S5A, B, and C. The result of broth microdilution method showed that the MIC of h-DCQDs was 0.05 μg/mL of *S. aureus* and *E. coli*, which was lower than levofloxacin-based carbon quantum dots. In addition, *S. aureus* stained with SYTO9/PI staining showed a lot of green fluorescence imaging of live bacteria, while the *S. aureus* incubated with h-DCQDs were stained with red fluorescence for the bacteria being killed, as showed in Fig. 5C. The similar result was observed in the gram-negative bacteria *E. coli* (Fig. S5D).

Compared with levofloxacin, h-DCQDs would be more effective to fight against *S. aureus* and *E. coli* within 50 passages (Fig. 6A and B). For levofloxacin hydrochloride (Levo-HCl), its minimum inhibitory concentration (MIC) against *S. aureus* (Fig. 6A) exhibited a notable increase starting at ~ 10 passages, with a sustained upward trend in subsequent passages (ultimately exceeding the initial value substantially). Against *E. coli* (Fig. 6B), the MIC of Levo-HCl began to rise after ~ 16 passages, followed by continuous elevation in later passages. These observations confirm that Levo-HCl readily drives the development of drug resistance in *S. aureus* and *E. coli*. In contrast, the MIC of h-DCQDs against both *S. aureus* and *E. coli* remained consistent with the initial level across 50 passages, showing no significant fluctuations. This result indicates that h-DCQDs have minimal potential to induce bacterial resistance, thereby exhibiting superior anti-resistance performance relative to Levo-HCl. Anti-biofilm activity is a necessary characteristic of antibacterial agents, because the infection will be aggravated or even repeated after bacteria form biofilm. The bacterial resistance and anti-biofilm properties of h-DCQDs were explored through the related experiment. The h-DCQDs could be used for anti-biofilm research by the CV staining results (Fig. 6C) and Confocal laser scanning microscopy (CLSM) images results (Fig. 6D). The quantitative data (Fig. 6C) showed that h-DCQDs had high inhibitory activity on the formation of bacterial biofilm. The biomass of *S. aureus* biofilm decreased with the increase of h-DCQDs concentration. When the concentration of h-DCQDs was 256 μg/mL, the maximum biofilm inhibition rate exceeded 99.99%. The CLSM images (Fig. 6D) showed that the inhibitory activity of h-DCQDs on the formation of bacterial biofilm was corresponding to CV staining results. CLSM was employed to capture fluorescent images, with SYTO9 (green fluorescence) labeling live bacteria and propidium iodide (PI, red fluorescence) labeling dead bacteria. The live/dead state of *S. aureus* was presented on the green/red fluorescence color. After the *S. aureus* incubation with saline, there were a lot of live bacteria in the biofilm and an obvious biofilm was formed. However, after the *S. aureus* treated with h-DCQDs at low or high concentration, only a little planktonic bacteria remain and bacteria become inactive completely, respectively. To evaluate the antibacterial and biofilm-eradicating potentials of levofloxacin, LCDs, D-his carbon quantum dots (h-CQDs), and D-his-modified carbon quantum dots (h-DCQDs) against *S. aureus*, the antibacterial activity of the four materials against planktonic *S. aureus* was investigated. We evaluated the antibacterial and anti-biofilm effects of bacteria using the live/dead bacterial staining method (Fig. S6 A), and determined the biomass of biofilms using the crystal violet assay (Fig. S6 B). *S. aureus* cells were treated with each material at a final concentration of 8 μg/mL for 8 h, followed by live/dead bacterial staining using the SYTO9/PI double-staining kit. Quantitative analysis of the fluorescent images revealed that the h-DCQDs treatment group exhibited the highest dead bacterial ratio (no less than 75%). This ratio was significantly higher than those of the levofloxacin, LCDs, and h-CQDs groups, indicating that h-DCQDs possessed superior bactericidal efficacy against planktonic *S. aureus* compared to the other three tested materials. In this set of experiments, *S. aureus* biofilms were treated with levofloxacin, LCDs, h-CQDs, and h-DCQDs (all at 8 μg/mL) for 24 h. Compared with h-CQDs and LCDs, the results show that h-DCQDs have significantly higher antibiofilm activities, confirming that D-his and its chiral properties enhance the biological activity of the material. Consistent with the planktonic antibacterial activity results, the h-DCQDs group achieved the highest biofilm clearance rate of 84.67 ± 0.03%. Quantitative comparison showed that this clearance rate was 2.3-fold higher than that of the levofloxacin group (44.22 ± 0.07%), 1.8-fold higher than that of the LCDs group (63.26 ± 0.12%), and 1.5-fold higher than that of the h-CQDs group (51.32 ± 0.33%). These data fully demonstrated the prominent biofilm-eradicating advantage of h-DCQDs over the other three materials. Collectively, the combined results of planktonic bacterial killing and biofilm eradication experiments consistently confirmed that h-DCQDs exhibited the most robust antibacterial activity against *S. aureus*.

Table 1
Shows MIC and MBC values of h-CQDs against different strains.

Strains	G^+/ G^-	MIC_d (μg/mL)	MBC_d (μg/mL)
S. aureus	G^+	0.025	0.100
MRSA	G^+	0.050	0.200
E. coli	G^-	0.025	0.100

3.4. Antibacterial mechanism of h-DCQDs

After evaluating the antibacterial activity of h-DCQDs *in vitro*, it is necessary to clarify the antibacterial mechanism of h-DCQDs. The positive surface of h-DCQDs can attach to bacteria with negative charges by electrostatic interaction. The DCFH-DA staining was used to evaluate the level of ROS in *S. aureus* or *E. coli* incubated with h-DCQDs, respectively (Fig. 7 A and B). The rosup was served as positive group, which could stimulate the production of ROS. The results showed that the fluorescence intensity of h-DCQDs group was higher than positive group, which meant the h-DCQDs could promote the production of ROS in bacteria. Meanwhile, the content in bacteria including nucleic acid and ATP obviously was leaked out after *S. aureus* or *E. coli* incubated with h-DCQDs, respectively (Fig. 7 C and D). The definition of membrane damaged and content leaked by ROS from the h-DCQDs stimulation to bacteria, which was certified by the membrane integrity of *S. aureus* or *E. coli* incubated with h-DCQDs in TEM images, respectively (Fig. 7 E). Based on the above results, the antibacterial mechanism of h-DCQDs was clarified to be the connection with bacteria by electrostatic interaction, the membrane destroyed by ROS and the content in bacteria leaked out.

3.5. Antibacterial activity of h-DCQDs in vivo

After evaluating the antibacterial activity of h-DCQDs *in vitro*, it is necessary to further evaluate its healing effect on infected wounds *in vivo* (Fig. 8). The *S. aureus* + *E. coli*-infected wound healing activity *in vivo* were evaluated to investigate the healing effect of the prepared h-DCQDs. Results showed the macroscopic different appearance between untreated group with levofloxacin hydrochloride and h-DCQDs on the 1st, 3rd, 5th, 7th and 10th day after operation (Fig. 8 A). The reduction of wound area and improvement of epithelial tissue were observed in all groups, while were more obvious in h-DCQDs group. The untreated group had mild infection and inflammation, while h-DCQDs groups were healing significantly after 10 days treatment. It was obvious that the wound healing with the treatment of h-DCQDs had almost been completed. The percentage of wound area was determined to the ratio of recovered wound area to induced wound area, which could quantify the wound healing process. After surgery, there was no difference in the percentage of initial wound area, which was served as 100% wound area percentage. On the 10th day after operation, the percentage of wound area of levofloxacin hydrochloride, h-DCQDs and untreated group reduced to varying degrees (Fig. S7 A). Compared with untreated group, h-DCQDs treatment can significantly reduce wound size. With the

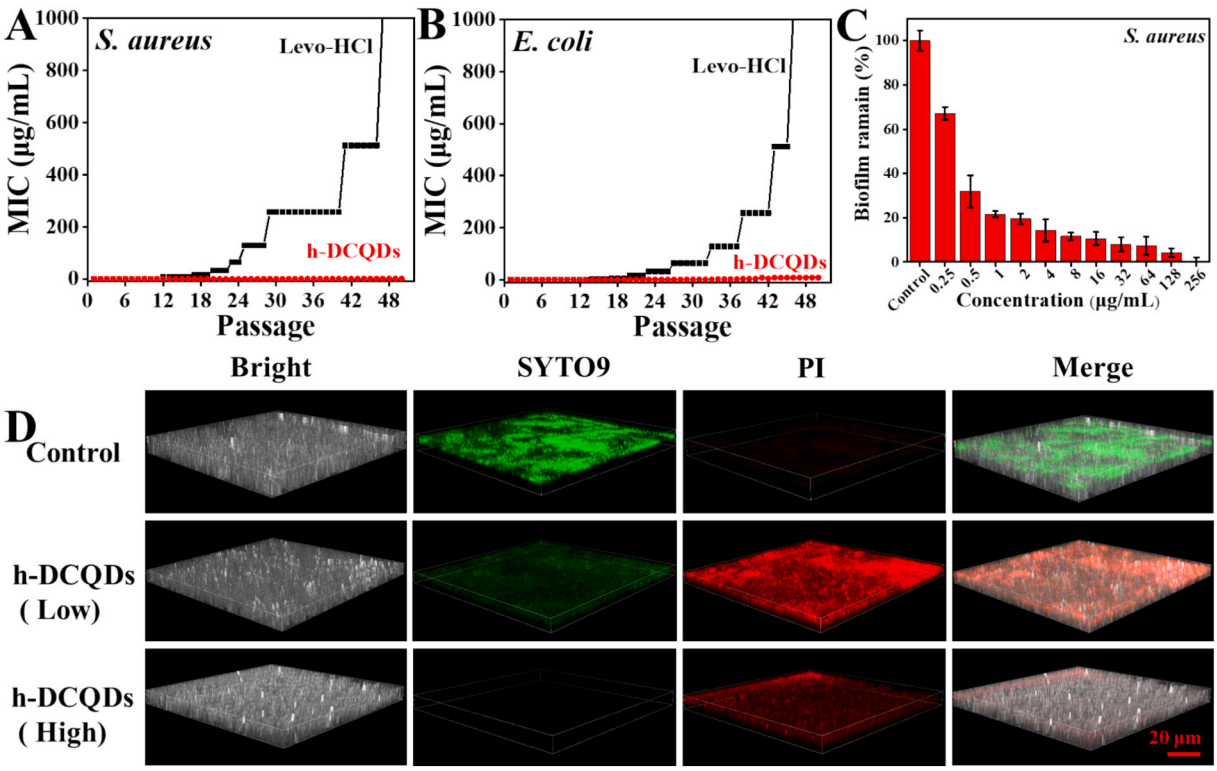

Fig. 6. The bacterial resistance and anti-biofilm of h-DCQDs. (A and B) The bacterial resistance of h-DCQDs against *S. aureus* and *E. coli*. (C) The quantitative data of CV staining and (D) the qualitative data of CLSM image about anti-biofilm inhibition of h-DCQDs at low/high concentration, scale bar: 20 μm.

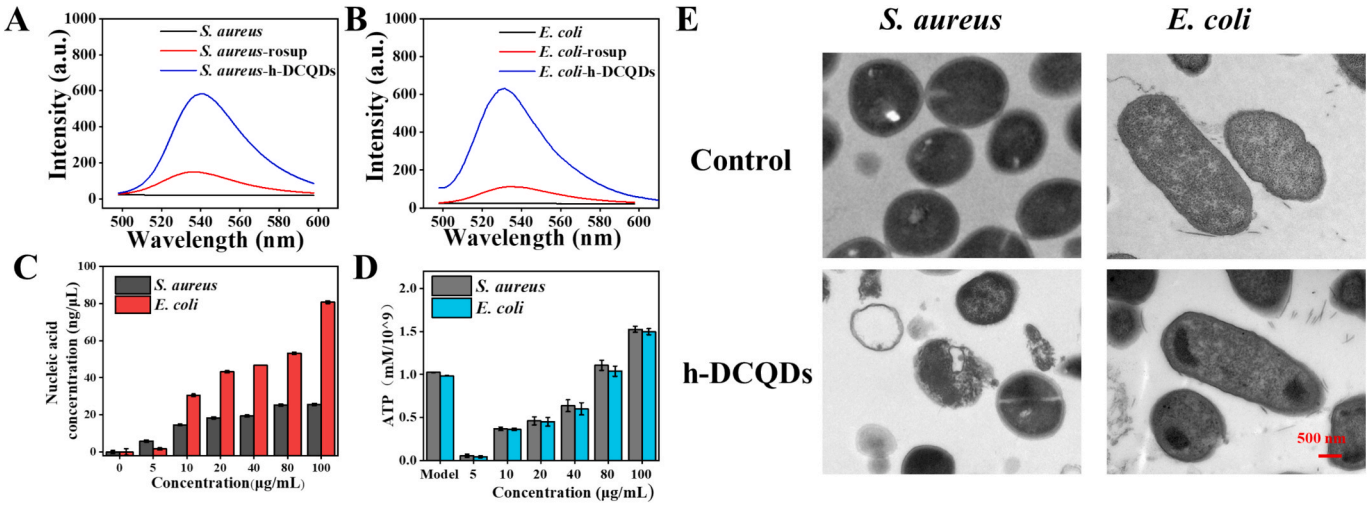

Fig. 7. The antibacterial mechanism of h-DCQDs. (A and B) The ROS assay of h-DCQDs against *S. aureus* and *E. coli*. (C) The nucleic acid leaking amount and (D) the ATP leaking amount of h-DCQDs against *S. aureus* and *E. coli*. (E) TEM images of h-DCQDs against *S. aureus* and *E. coli*., scale bar: 500 nm.

decrease of wound area of mice, the decreased weight gradually recovered to the trend of slow growth (Fig. S7 B). Pathological basic staining analysis of skin wounds were carried out by hematoxylin-eosin staining (Fig. 8 B), the image of hematoxylin-eosin staining of h-DCQDs group showed a shape more similar with healthy skin than other groups, including few hypertrophic scars, thin epidermis and almost normal hair growing on the wound surface. However, untreated negative group showed plenty of monocytes and granulocytes. The reduction of bacterial content in wounds based on CFU counts was evaluated (Fig. S7 C). After 10 days' treatment with normal saline, there was essentially no antimicrobial effect. However, h-DCQDs and levofloxacin hydrochloride treatment groups have no bacterial residues. The results are consistent with the results of *in vitro* bactericidal activity determination. These data showed the bacterial viability of h-DCQDs and levofloxacin hydrochloride treatment group decreased significantly, which were consistent with the results of bactericidal activity *in vitro*.

3.6. Biocompatibility of h-DCQDs

RAW264.7 cells were used for MTT assay to evaluate the cytotoxicity of h-DCQDs towards mammalian cells *in vitro*. As shown in Fig. S8 A, h-DCQDs showed no obvious cytotoxicity at 0–800 μg/mL and even more than 100% of RAW 264.7 cell viability, which meant the toxicity of h-DCQDs to RAW264.7 cells could be neglected. Meanwhile, hemolysis

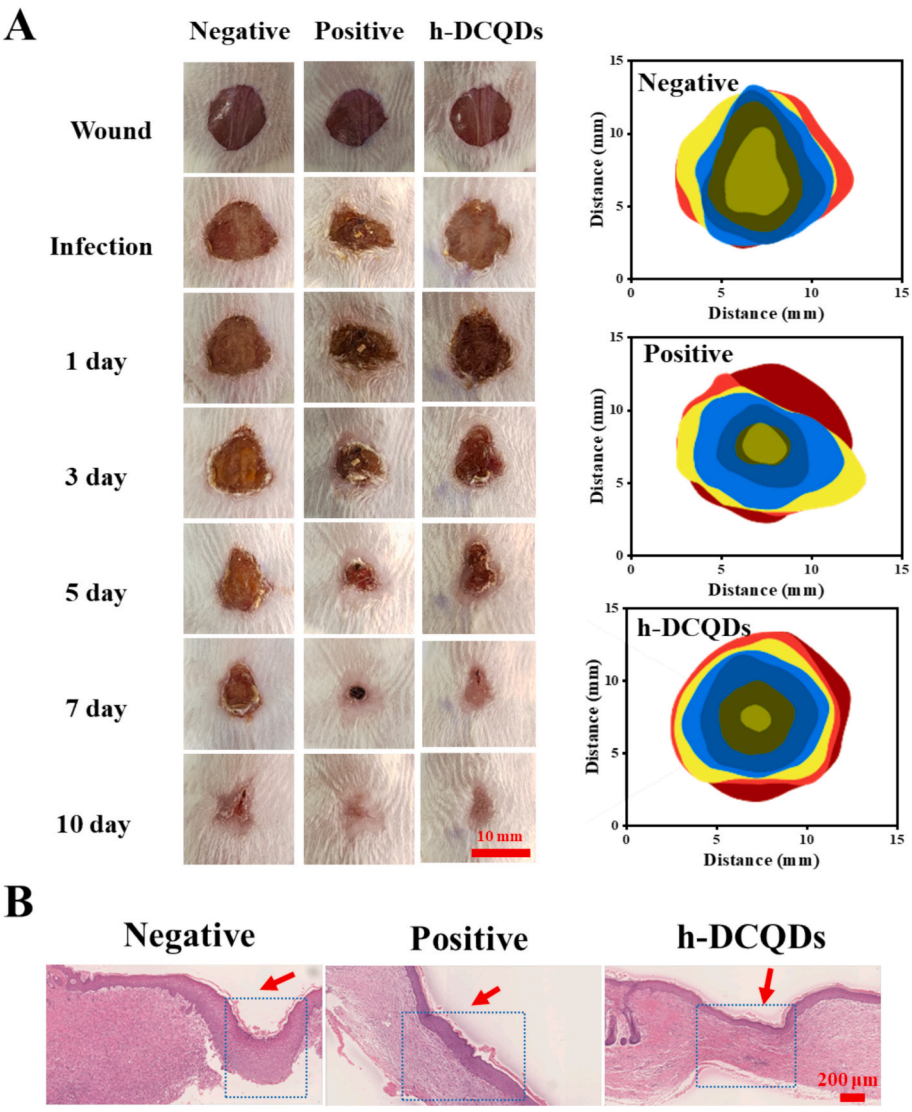

Fig. 8. The antibacterial activity of h-DCQDs *in vivo*. (A) Photographs of healing process of wounds infected with *S. aureus* + *E. coli* in normal saline, levofloxacin hydrochloride and h-DCQDs group. The contour map in the illustration indicates the healing trend of the wound edge, scale bar: 10 mm. (B) H&E staining images of wound tissues from the three treatment groups. The arrow indicates the area of inflammatory cell infiltration and tissue repair, scale bar: 200 μm.

test was conducted to verify whether h-DCQDs could cause hemolysis and further evaluated blood compatibility. As shown in Fig. S8 B, the red blood cells solution was turned red after added to water, indicating that red blood cells were broken. However, when sterilized saline and saline containing h-DCQDs at 0–800 μg/mL were added the red blood cells, the solution was still colorless. The red blood cells all were deposited on the bottom of the centrifuge tube after centrifugation. The results of MTT assay and hemolysis test of h-DCQDs all certificated the non-toxicity of h-DCQDs *in vitro*, which indicated that h-DCQDs could not cause red blood cell rupture and hemolysis under physiological conditions. Although the cytotoxicity of h-DCQDs was minimal *in vitro*, it was necessary to further investigate and evaluate the toxicity of h-DCQDs *in vivo*. The toxicity of h-DCQDs to mice were investigated by dermal administration of h-DCQDs solution for 10 days. Within 10 days, the activities, diet and mental state of all mice were normal. After 10 days, the toxicity of h-DCQDs to the main organs of mice *in vivo* was compared and evaluated from the pathological aspect, as shown in Fig. S8 C. The histological sections of heart, liver, spleen, lung and kidney with H&E

Table 2
Routine blood test results of h-DCQDs *in vivo*. The results obtained were expressed as average ± standard deviation from at least three repeats.

Parameter	Control	Error bar	h-DCQDs	Error bar	Unit	Reference range
WBC	2.773333	0.630899	2.96	0.816639	$10^{\wedge}9$/L	0.80——10.60
Neu#	0.7	0.166433	0.896667	0.156312	$10^{\wedge}9$/L	0.23——3.60
Lym#	1.43	0.177764	1.17	0.848705	$10^{\wedge}9$/L	0.60——8.90
Mon#	0.483333	0.281129	0.46	0.144222	$10^{\wedge}9$/L	0.04——1.40
Eos#	0.1	0.03	0.116667	0.025166	$10^{\wedge}9$/L	0.00——0.51
Bas#	0.06	0.017321	0.316667	0.119304	$10^{\wedge}9$/L	0.00——0.12
RBC	6.546667	2.128294	7.89	1.085956	$10^{\wedge}12$/L	6.50——11.50
HGB	110.6667	33.62043	140.3333	4.163332	g/L	110——165
PLT	711.3333	166.5843	591.6667	182.9381	$10^{\wedge}9$/L	400——1600

color showed that there was no significant difference between h-DCQDs group and control group. In addition, blood routine results were consistent with the above results, as shown in Table 2. These results indicated that the h-DCQDs could be further inferred that h-DCQDs did not produce toxicity *in vivo* and *in vitro*. Further safety research needs exploration in further work.

4. Conclusions

The experimental results showed that h-DCQDs had remarkable antibacterial activity. The h-DCQDs would be applied to solve bacterial infections, including resisting the formation of bacterial drug-resistant and biofilm. The unique size and chirality characteristics of h-DCQDs enabled them to penetrate and eliminate the biofilm, thus overcoming intractable infection. The h-DCQDs with positive charge and chirality could gather in the infected target more effectively and combine with bacteria with negative charges on the surface more effectively, resulting in broad-spectrum antibacterial effect and fluorescent bioimaging. The h-DCQDs with antibacterial activity can promote infected wound healing *in vivo*, which was used to treat the animal wound model of bacterial infection. Compared with the, h-DCQDs had a remarkable therapeutic effect on the regression of inflammation and the reconstruction of skin tissue. It introduces a novel strategy for precisely engineering microbe surfaces and provides new avenues for tracking and treating bacterial infections.

Ethical approval statement

This study was carried out in accordance with the recommendations of the Animal Care and Use Committee of Huaqiao University (approval number: A2023004). All animal procedures were performed under the approved ethical protocol, and every effort was made to minimize animal suffering and reduce the number of animals used in the study.

CRediT authorship contribution statement

Lina Wu: Writing – review & editing, Writing – original draft, Visualization, Validation, Supervision, Software, Resources, Project administration, Methodology, Investigation, Funding acquisition, Formal analysis, Data curation, Conceptualization. **Xiaoyun Lin:** Writing – review & editing, Funding acquisition. **Lingxuan Sun:** Software, Methodology. **Jinpin Zhang:** Software, Methodology. **Jinxi Liu:** Methodology, Investigation. **Shuixin Liang:** Methodology, Investigation. **Wei Luo:** Software, Investigation. **Jiaxin Xue:** Software, Methodology, Investigation. **Yujun Wen:** Software, Investigation. **Tiantian Wang:** Software. **Ailin Liu:** Writing – review & editing. **Yong Diao:** Funding acquisition, Data curation, Conceptualization. **Xianquan Feng:** Writing – review & editing, Methodology, Funding acquisition. **Liqing Lin:** Writing – review & editing, Funding acquisition, Conceptualization.

Declaration of competing interest

The authors declare that they have no known competing financial interests or personal relationships that could have appeared to influence the work reported in this paper.

Acknowledgments

The authors gratefully acknowledge the financial support of the National Natural Science Foundation of China (Grant No. 82504646 and 82273981), Natural Science Foundation of Fujian Province (Grant No. 2024J08094), Joint Funds for the innovation of science and Technology, Fujian province (Grant No. 2024Y9044 and 2024Y9646) and Scientific Research Funds of Huaqiao University (Grant No. 22BS129). The authors acknowledge the assistance of the Instrumental Analysis Center of Huaqiao University, Liu from Scientific Compass (www.shiyanjia.com), and the Public Technology Service Center of Fujian Medical University for technical assistance.

Appendix A. Supplementary data

Supplementary data to this article can be found online at https://doi.org/10.1016/j.matdes.2026.115843.

Data availability

Data will be made available on request.

References

[1] J. Cohn, M. Mendelson, S.S. Kanj, N. Shafiq, I. Boszczowski, R. Laxminarayan, Accelerating antibiotic access and stewardship: a new model to safeguard public health [J], Lancet Infect. Dis. 9 (2024) 584–590, https://doi.org/10.1016/s1473-3099(24)00070-7.
[2] A.J. Bumler, The coming microbial crisis: our antibiotic bubble is about to burst [J], Science 385 (6715) (2024) 3473, https://doi.org/10.1126/S3473.
[3] J.A. Doolan, G.T. Williams, K.L.F. Hilton, R. Chaudhari, J.S. Fossey, B.T. Goult, Advancements in antimicrobial nanoscale materials and self-assembling systems [J], Chem. Soc. Rev. 51 (2022) 8696–8755, https://doi.org/10.1039/D1CS00915J.
[4] S.S. Wang, D.P. Wang, G.L. Wang, M.L. Zhang, Y.R. Sun, J.X. Ding, Antibacterial carbon dots [J], Mater. Today Bio 30 (2025) 101383, https://doi.org/10.1016/j.mtbio.2024.101383.
[5] S.P. Pei, J. Zhang, M.P. Gao, D.Q. Wu, Y.X. Yang, A facile hydrothermal approach towards photoluminescent carbon dots from amino acids [J], J. Colloid Interface Sci. 439 (1) (2015) 129–133, https://doi.org/10.1016/j.jcis.2014.10.030.
[6] Y. Zhang, S.T. Zhang, B.C. Tan, L. Guo, H.T. Li, Solvothermal synthesis of functionalized carbon dots from amino acid as an eco-friendly corrosion inhibitor for copper in sulfuric acid solution [J], J. Colloid Interface Sci. 604 (15) (2021) 1–14, https://doi.org/10.1016/j.jcis.2021.07.034.
[7] S.M. Ardekani, A. Dehghani, P. Ye, K.A. Nguyen, V.G. Gomes, Conjugated carbon quantum dots: potent nano-antibiotic for intracellular pathogens [J], J. Colloid Interface Sci. 552 (15) (2019) 378–387, https://doi.org/10.1016/j.jcis.2019.05.067.
[8] C. Zhong, N.Y. Zhu, Y.W. Zhu, T.Q. Liu, S.H. Gou, J.Q. Xie, J. Yao, J.M. Ni, Antimicrobial peptides conjugated with fatty acids on the side chain of D-amino acid promises antimicrobial potency against multidrug-resistant bacteria [J], Eur. J. Pharm. Sci. 141 (1) (2020) 105123, https://doi.org/10.1016/j.ejps.2019.105123.
[9] W.Z. Song, X.X. Wang, S.L. Nong, M.R. Wang, S.M. Kang, F. Wang, L. Xu, D-cysteine-derived carbon dots for selective discrimination, imaging, and synergistic elimination of gram-positive bacteria and fungi [J], Adv. Funct. Mater. 34 (38) (2024), https://doi.org/10.1002/adfm.202402761.
[10] P.J. Renick, A. Mulgaonkar, C.M. Co, C.Y. Wu, N. Zhou, A. Velazquez, J. Pennington, A. Sherwood, H. Dong, L. Castellino, O.K. Öz, L.P. Tang, X.K. Sun, Imaging of actively proliferating bacterial infections by targeting the bacterial metabolic footprint with d- [5-11C]-glutamine [J], ACS Infect. Dis. 7 (2) (2021) 347–361, https://doi.org/10.1021/acsinfecdis.0c00617.
[11] S.S. Wei, C.Z. Wang, Y.C. Wang, X.Y. Yin, K.X. Hu, M. Liu, G.Y. Sun, L.H. Lu, Chiral carbon dots derived from tryptophan and threonine for enantioselective sensing of L/D-Lysine [J], J. Colloid Interface Sci. 662 (1) (2024) 48–57, https://doi.org/10.1016/j.jcis.2024.02.063.
[12] F. Li, S. Li, X.C. Guo, Y.H. Dong, C. Yao, Y.P. Liu, Y.G. Song, X.L. Tan, L.Z. Gao, D. Y. Yang, Chiral carbon dots mimicking topoisomerase I to mediate the topological rearrangement of supercoiled DNA enantioselectively [J], Angew. Chem. Int. Ed. Engl. 59 (27) (2020) 11087–11092, https://doi.org/10.1002/anie.202002904.
[13] S.Y. Zhao, X.R. Chen, J.Y. Su, P.T. Zhao, C.L. Si, T. Xu, C. Huang, X.P. Song, Interaction of lignin and xylan in the hydrothermal synthesis of lignocellulose-based carbon quantum dots and their application in *in-vivo* bioimaging [J], Int. J. Biol. Macromol. 222 (1) (2022) 1876–1887, https://doi.org/10.1016/j.ijbiomac.2022.09.276.
[14] F.B. Wang, M.H. Xiao, J. Qi, L. Zhu, Paper-based fluorescence sensor array with functionalized carbon quantum dots for bacterial discrimination using a machine learning algorithm [J], Anal. Bioanal. Chem. 416 (13) (2024) 3139–3148, https://doi.org/10.1007/s00216-024-05262-4.
[15] L. Miao, W.W. Liu, Q.L. Qiao, X.L. Li, Z.C. Xu, Fluorescent antibiotics for real-time tracking of pathogenic bacteria [J], J. Pharm. Anal. 10 (5) (2020) 444–451, https://doi.org/10.1016/j.jpha.2020.09.003.
[16] S.A.R. Naqvi, S. Roohi, H. Sabir, S.A. Shahzad, A. Aziz, R. Rasheed, Susceptibility of 99mTc-ciprofloxacin for common infection causing bacterial strains isolated from clinical samples: an in vitro and in vivo study [J], Appl. Biochem. Biotechnol. 188 (2) (2018) 424–435, https://doi.org/10.1007/s12010-018-2915-z.
[17] L. Jiang, H. Cai, W.W. Zhou, Z.J. Li, L. Zhang, H. Bi, RNA-targeting carbon dots for live-cell imaging of granule dynamics [J], Adv. Mater. 35 (1) (2023) 2210776, https://doi.org/10.1002/adma.202210776.
[18] I. Zare, S.Z. Nasab, A. Rahi, A. Ghaee, M. Koohkhezri, M.R. Farani, H.M. Gholipour, A.H. Atabaki, M.R. Hamblin, E. Mostafavi, H. Kang, Antimicrobial carbon materials-based quantum dots: from synthesis strategies to antibacterial properties

for diagnostic and therapeutic applications in wound healing [J], Coord. Chem. Rev. 522 (1) (2025) 216211, https://doi.org/10.1016/j.ccr.2024.216211.
[19] Y. Wu, H. Wei, H.C. van der Mei, J. de Vries, H.J. Busscher, Y. Ren, Inheritance of physico-chemical properties and ROS generation by carbon quantum dots derived from pyrolytically carbonized bacterial sources [J], Mater. Today Bio 12 (1) (2021) 100151, https://doi.org/10.1016/j.mtbio.2021.100151.
[20] L.N. Wu, Y.J. Yang, L.X. Huang, Y. Zhong, Y. Chen, Y.R. Gao, L.Q. Lin, Y. Lei, A. L. Liu, Levofloxacin-based carbon dots to enhance antibacterial activities and combat antibiotic resistance [J], Carbon 186 (1) (2022) 452–464, https://doi.org/10.1016/j.carbon.2021.10.020.
[21] B. Rooj, U. Mandal, A review on characterization of carbon quantum dots [J], Vietnam J Chem 61 (6) (2023) 693–718, https://doi.org/10.1002/vjch.202300022.
[22] R.F. Mehrnaz, M. Marziyeh, N. Maryam, R. Aram, M. Sajad, H. Saman, A comparative study of structural and catalytic activity alterations in firefly luciferase induced by carbon quantum dots containing amine and carboxyl functional groups [J], Int. J. Biol. Macromol. 260 (2024) 129503, https://doi.org/10.1016/j.ijbiomac.2024.129503.
[23] S. Zeinab, J.M. Mohammad, J.M. Atieh, R. Aram, S. Karolina, N. Maryam, A label-free sensor array based on carbon quantum dots for detection of α-synuclein oligomers in saliva [J], Anal. Chem. 96 (30) (2024) 12246–12253, https://doi.org/10.1021/acs.analchem.4c00874.
[24] T. Zhang, S.Y. Hou, X.M. Huo, H.M. Li, H.Q. Shi, X. Wang, C.B. Liu, Y.Z. Guo, Two-pronged approach: synergistic tuning of the surface and carbon core to achieve yellow emission in lignin-based carbon dots [J], ACS Appl. Mater. Interfaces 15 (36) (2023) 42823–42835, https://doi.org/10.1021/acsami.3c07075.
[25] L. Zhan, P. Hou, N. Chen, Y.F. Li, C.M. Li, C.Z. Huang, Amino-terminated carbon dots for imaging Golgi apparatus polarity in live cells [J], Chem. Eng. J. 475 (1) (2023) 145613, https://doi.org/10.1016/j.cej.2023.145613.
[26] C.F. Zhao, L.N. Wu, X.W. Wang, S.H. Weng, Z.P. Ruan, Q.C. Liu, L.Q. Lin, X.H. Lin, Quaternary ammonium carbon quantum dots as an antimicrobial agent against gram-positive bacteria for the treatment of MRSA-infected pneumonia in mice [J], Carbon 163 (15) (2020) 70–84, https://doi.org/10.1016/j.carbon.2020.03.009.
[27] L. Liu, S. Anwar, H.Z. Ding, M.S. Xu, Q. Yin, Y.Z. Xiao, X.Y. Yang, M.Q. Yan, H. Bi, Electrochemical sensor based on F, N-doped carbon dots decorated laccase for detection of catechol [J], J. Electroanal. Chem. 840 (2019) 84–92, https://doi.org/10.1016/j.jelechem.2019.03.071.
[28] R.F. Mehrnaz, M. Marziyeh, N. Maryam, M. Sajad, A. Mohabbat, C. Klara, H. Saman, R. Aram, Chirality governs the structure and activity changes of Photinus pyralis firefly luciferase induced by carbon quantum dots [J], Nanoscale Adv. 6 (24) (2024) 6154–6165, https://doi.org/10.1039/d4na00621f.
[29] W.Y. Ma, B.L. Wang, Y.G. Yang, J.Y. Li, Photoluminescent chiral carbon dots derived from glutamine [J], Chinese Chem Let 32 (12) (2021) 3916–3920, https://doi.org/10.1016/j.cclet.2021.05.021.
[30] A. Rezaei, H.J. Zheng, M. Shiva, S. Saadi, A. Ramazani, Chiral pseudohomogeneous catalyst based on amphiphilic carbon quantum dots for the enantioselective kharasch–sosnovsky reaction [J], ACS Appl. Mater. Interfaces 15 (47) (2023) 54373–54385, https://doi.org/10.1021/acsami.3c10756.
[31] Q. Xin, Q. Liu, L.L. Geng, Q.J. Fang, J.R. Gong, Chiral nanoparticle as a new efficient antimicrobial nanoagent [J], Adv. Healthc. Mater. 6 (4) (2016) 1601011, https://doi.org/10.1002/adhm.201601011.